High-altitude Inspection Technology of Substation Based on Fusion of Unmanned Aerial Vehicle and Multiple Sensors

Xiaohua Yang,[1] Xiao Ye,[2] Jianing Cao,[2*] Rong Yan,[2] Xiaojue Guo,[3] and Jisheng Huang[4]

[1]Measurement Center, Yunnan Power Grid Co., Ltd., Kunming 650051, China
[2]Faculty of Civil Aviation and Aeronautics, Kunming University of Science and Technology,
Kunming 650500, China
[3]Kunming ZhiYuan Measurement & Control Technology Co., Ltd., Kunming 650500, China
[4]Lincang Power Supply Bureau, Yunnan Power Grid Co., Ltd., Lincang 677099, China

With the continuous development of the power grid industry, the difficulty of substation operation and maintenance is also increasing. Because of its high mobility and low destructiveness, a rotary-wing unmanned aerial vehicle (UAV) can achieve effective detection and avoid the difficulty and poor accuracy of high-altitude inspection of substations. Owing to the ability of a UAV to integrate various sensors, such as visible light imaging sensors, thermal imaging sensors, and self-positioning sensors, it can ensure its own safety and that of the equipment to be tested during the inspection. Thus, in this paper, we study the application of rotary-wing multi-sensor UAVs in the high-altitude inspection of substations. Firstly, we establish a UAV inspection and autonomous detection model involving electromagnetic and other environmental influences. This model considers substation environmental restrictions, UAV physical constraints, and the limitations of sensor detection, and it is combined with a mobile edge computing platform. Secondly, we design an improved path planning algorithm combining the floating algorithm and the rapidly exploring random trees (RRT) algorithm and introduce improved strategies such as the Cauchy mutation strategy and Lèvy flight strategy to reduce the blindness of the algorithm search. Finally, by conducting simulation experiments and comparing the designed algorithm with traditional algorithms such as the ant colony algorithm, genetic algorithm, and simulated annealing algorithm, we verify the feasibility of the model and algorithm. The results of this study provide practical assistance to promote the automation and intelligence of substation inspection.

1. Introduction

In recent years, the development of the power grid industry has tended to be informative and intelligent.[(1)] As an important node in the power grid, the operation of substations directly determines the result of power distribution, thus affecting the operation of the whole power grid.

Therefore, the inspection of substations is crucial. With the advancement of smart grids, the requirements for lean substation equipment operation and maintenance are also increasing, requiring the development of intelligent substation inspection.

Traditional substation inspection involves regular inspection and observation by maintenance personnel, which is time-consuming and limited by the difficulty of observing faults in high-altitude equipment, thus affecting the safety of the substation. Unmanned aerial vehicles (UAVs) are gradually being adopted by the power grid industry due to their high mobility and high-altitude views, greatly reducing the workload of maintenance personnel.[2] Meanwhile, the continuous development of image sensor technology has made the intelligent diagnosis and identification of faults and defects in grid equipment more accurate and robust. Therefore, the intelligent inspection of substations based on drones and sensors is gradually becoming mainstream.[3] In addition, edge computing technology also has applications in the power grid industry,[4] which facilitates the processing of large amounts of inspection data and further improves the mobility and convenience of UAV inspections.[5] In summary, UAV technology, sensor technology, and edge computing technology provide the software and hardware basis for intelligent substation inspection, and integrating the three is the key to development.[6]

The accuracy of UAV-based industrial applications depends mainly on the effectiveness of the mathematical model developed and has been a hot topic of researchers.[7] Among them, Tran *et al*.[8] designed a UAV trajectory model with the minimum total energy consumption while satisfying the timeout requirement and energy budget as the optimization objective. Yu *et al*.,[9] on the other hand, studied plant protection tasks carried out by UAVs and reduced operational costs by constructing shortest-path and least-number models. Liu *et al*.[10] constructed energy-efficient and time-efficient minimization models and completed inventory operations in indoor warehouses, using rotary-wing UAVs to improve operational efficiency. In summary, some results have been achieved in UAV trajectory planning, but there have been few studies on substation inspection, most of which have been based on ground robots,[11–13] which have high space constraints and operational costs. Therefore, in this paper, we construct a substation inspection path planning model based on a rotary-wing UAV in fusion with multiple sensors, with the sensors themselves providing mathematical support for the UAV substation inspection trajectory planning.

The most critical aspect of substation inspection based on UAVs is the planning of UAV inspection paths.[14] Heuristic and metaheuristic algorithms have been used in UAV trajectory planning, where the rapidly exploring random trees (RRT) algorithm[15] and A* algorithm[16] exhibit good results. However, for high-dimensional path planning problems involving complex constraints, a single classical path planning algorithm can fall into a local optimum. For this reason, various improvement strategies have been introduced to enhance the global optimization capability of algorithms. Pan *et al*.[17] improved the golden eagle optimization algorithm by using two strategies: personal example learning and mirror reflection learning. Chai *et al*.[18] improved the difference algorithm by using multiple swarm strategies, new adaptive strategies, and interactive mutation strategies to improve its ability to solve high-dimensional problems. Wang *et al*.[19] improved the jump-out and revisit mechanisms of the distributed particle swarm optimization algorithm (PSO) to reduce the blindness of the algorithm search. In summary, a

feasible research method is to improve a heuristic or metaheuristic algorithm to obtain better path planning results. The mayfly algorithm (MA), an emerging metaheuristic algorithm,[20] had its initial applications in various fields and it has been shown to have a strong capability for solving high-dimensional optimization problems.[21] Therefore, we improve the RRT algorithm based on MA to reduce the blindness of its search while retaining its ability to solve high-dimensional problems, thus increasing the speed of the solution while ensuring its accuracy.

In this paper, we study the problem of substation inspection based on a rotary-wing UAV fused with multiple sensors, build an intelligent substation inspection system architecture, and establish a UAV inspection model with inspection distance, time, and energy consumption as optimization indexes to enable the UAV to complete the substation inspection task. We also improve the RRT algorithm based on the metaheuristic algorithm to plan UAV inspection trajectories and promote the intelligence of substation inspection. To summarize, the contributions of this paper are as follows.

1. We introduce a substation inspection task process involving sensor technology, edge computing technology, and a UAV and construct the architecture of an intelligent substation inspection system.
2. We construct a UAV inspection model involving UAV physical constraints, sensor operation constraints, and inspection task constraints and establish the UAV inspection distance, time, and energy consumption as indicators to ensure efficient UAV substation inspection.
3. We improve the RRT algorithm through MA to enhance its search speed and accuracy to achieve effective UAV substation inspection trajectory planning.
4. We establish a 3D simulation environment model. We use PSO, the genetic algorithm (GA), MA, and the proposed improved mayfly algorithm based on Cauchy mutation strategy and Lèvy flight strategy (ICLMA) to carry out simulation experiments, and we compare the results to evaluate the developed model and algorithm.

The rest of this paper is as follows. In Sect. 2, the substation inspection task flow and intelligent substation inspection system architecture based on a rotary-wing UAV fused with multiple sensors are introduced. In Sect. 3, a UAV inspection model with inspection distance, time, and energy consumption as the optimization indexes is established. In Sect. 4, an improved path planning algorithm combining MA and the RRT algorithm is designed. In Sect. 5, simulation experiments are carried out and the results are analyzed. Finally, Sect. 6 concludes the paper.

2.   Inspection Task Description

The substation contains primary equipment such as transformers, high-voltage circuit breakers, and lightning arresters (equipment that directly generates, transmits, distributes, and uses electric energy) and secondary equipment such as relay protection devices, measurement, control devices, and metering devices (equipment that measures, controls, monitors, and protects the primary equipment). The inspection of the substation requires the operators to check the above equipment, detect abnormalities, and repair the abnormal equipment to ensure the standard and safe operation of the substation. The intelligent inspection of a substation based on

a rotary-wing UAV requires the inspection trajectory of the UAV to cover all the equipment under inspection to capture images of the equipment to be inspected using visual sensors such as IR cameras and to transmit the image information to a mobile edge computing platform using wireless communication technology. The platform detects abnormalities of the equipment through a feature recognition algorithm and, finally, streams the data back to the computing center. The rotary-wing UAV carries out the intelligent inspection of substations by employing multiple heterogeneous sensors, significantly reducing inspection blind areas while safeguarding inspection accuracy, and inspection data are effectively collected and processed by sensor technology and edge computing technology through the following specific processes.

1. The computing center plans inspection paths based on a 3D distribution model of the substation equipment.
2. On the basis of the inspection route, the UAV realizes autonomous flight by carrying a self-positioning real-time kinematic (RTK) module. When it reaches the inspection point, the UAV collects visible images, IR images, and video recording information of the equipment to be inspected through its IR thermal imaging camera and an ordinary optical camera.
3. The UAV transmits the inspection information to the preset mobile edge server in the substation through the equipped map transmission module. The server uses the preset information processing algorithm for abnormality detection and transmits the detection results to the computing center.

3.   UAV Inspection Model

The development of the intelligent substation inspection system should be based on the UAV platform, and the accuracy of UAV inspection depends on the comprehensiveness of the established inspection model. Reasonable assumptions will greatly simplify the calculation in inspection task planning. The following is a detailed description of the established UAV inspection model. Figure 1 shows the main system architecture for inspection using UAVs.
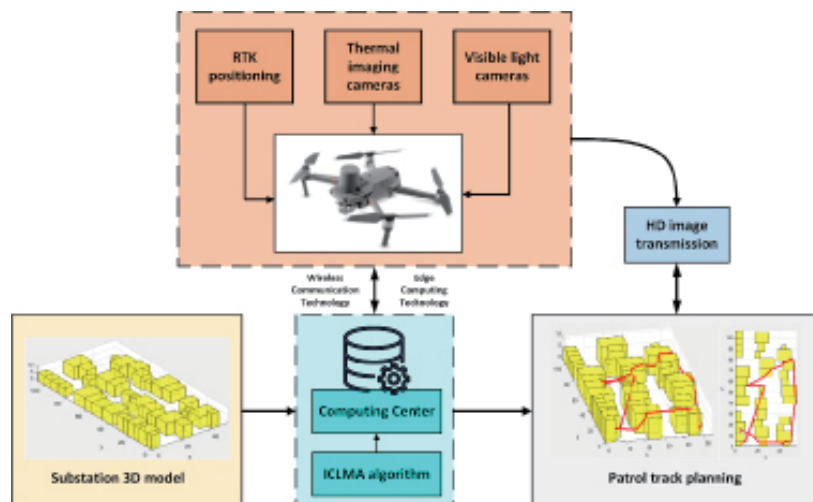
Fig. 1.   (Color online) Architecture of intelligent substation inspection system.

3.1   Model assumptions

Because of its high maneuverability, a rotary-wing UAV has effective targeting in inspection, and the analysis of its complex dynamics increases the difficulty of establishing inspection models. We assume the following in our model.
1. Owing to the high mobility of the rotary UAV, the acceleration or deceleration phase can be ignored because of its short duration compared with the total flight time, i.e., the flight of the UAV is considered uniform, and the uniform flight speed is specified as 80% of the maximum flight speed.
2. The rotary-wing UAV only operates when the wind strength is lower than the safety threshold, and the cm-level hovering error generated by the wind is offset by the RTK module and gimbal carried by the UAV, allowing the impact of wind on inspection to be ignored.
3. The energy consumed by the UAV to adjust its attitude is negligible.[22]

3.2   Model building

Firstly, a reference point O in the substation is selected as the local coordinate origin of the substation, with the X axis pointing to the geographic North Pole, the Y axis pointing east, and the Z axis pointing vertically downward. Using the 3D coordinate system of the substation environment, the UAV trajectory can be represented by a series of ordered coordinates. Therefore, an inspection can be expressed as $S \rightarrow T \rightarrow E$, where $S = (x_0, y_0, z_0)$ indicates the coordinates of the starting point of the trajectory where the UAV starts inspection, $E = (x_e, y_e, z_e)$ denotes the coordinates of the endpoint of the UAV inspection trajectory, and $T = \{(x_i, y_i, z_i) \mid \forall i \in \{1, 2, \cdots, n\}\}$ indicates the set of coordinates of the centers of the equipment to be inspected. Also, the coordinates of the highest and lowest points of the equipment are expressed by $I_i^{max} = (x_i, y_i, h_i^{max})$ and $I_i^{min} = (x_i, y_i, h_i^{min})$, respectively. The location of drone U is denoted as $U = (x_U, y_U, z_U)$ and the location of the mobile edge server MES in the substation is denoted as $MES = (x_{MES}, y_{MES}, z_{MES})$. On the basis of this mathematical description of the inspection task, the inspection model is established as shown below.

The trajectory of the UAV between any two nodes can be represented as a vector and can be projected to the A-plane and S-axis direction. The flight distance of the UAV between any two nodes can be characterized by the Euclidean parameterization of the vector corresponding to the track segment as follows.

$$\overrightarrow{J_{ij}} = \overrightarrow{J_{ij}^H} + \overrightarrow{J_{ij}^V}, \quad \forall i, j \in \{S, T, E\} \tag{1}$$

$$D_{ij} = \left\|\overrightarrow{J_{ij}}\right\|_2 = \left\|\overrightarrow{J_{ij}^H}\right\|_2 + \left\|\overrightarrow{J_{ij}^V}\right\|_2, \quad \forall i, j \in \{S, T, E\} \tag{2}$$

$$\left\|\overrightarrow{J_{ij}^H}\right\|_2 = \sqrt{(x_j - x_i)^2 + (y_j - y_i)^2}, \quad \forall i, j \in \{S, T, E\} \tag{3}$$

$$\left\| \overrightarrow{J_{ij}^{V}} \right\|_{2} = \sqrt{(z_j - z_i)^2}, \quad \forall i,j \in \{S,T,E\} \tag{4}$$

Here, $\overrightarrow{J_{ij}}$ is the track vector between any two nodes, and $\overrightarrow{J_{ij}^{H}}$ and $\overrightarrow{J_{ij}^{V}}$ are the projection vectors of the track vector in the horizontal and vertical directions, respectively. In Eq. (2), D_{ij} is the length of the track between any two nodes and $\|\bullet\|_2$ represents the 2-parametric number of the vector, i.e., the Euclidean parametric number, which is calculated using Eqs. (3) and (4).

3.2.1   Inspection distance index

The 0–1 variable is introduced as shown in Eq. (5), which takes a value of one when the UAV travels from point i to point j and zero when it does not. We combine Eqs. (2) and (5) to obtain the inspection distance index in Eq. (6), where D_{ij} is the flight distance between track points i and j, and the sum of its product with the decision variable X_{ij} represents the total length of the track points passed by the UAV.

$$X_{ij} = \begin{cases} 1, & \text{UAV from point } i \text{ to point } j \\ 0, & \text{Otherwise} \end{cases} \tag{5}$$

$$UD = \sum D_{ij} \times X_{ij}, \quad \forall i,j \in \{S,T,E\} \tag{6}$$

3.2.2   Inspection time indicator

Similarly to the UAV trajectory representation, the UAV flight speed is projected onto the A-plane and the S-axis direction, then the UAV inspection flight time is determined by the magnitude of the velocity vector of the trajectory length. The UAV executes the preset inspection task after reaching the inspection point, and the inspection task execution time includes the attitude adjustment time of the UAV, the working time of the image sensor, and the information transmission time of the map transmission module. The inspection time index is obtained by combining the inspection flight time and task execution time, as shown in Eq. (12).

$$\overrightarrow{V_U} = \overrightarrow{V_H} + \overrightarrow{V_V} \tag{7}$$

$$TF_{ij} = \frac{\left\| \overrightarrow{J_{ij}^{H}} \right\|_2}{\left| \overrightarrow{V_H} \right|} + \frac{\left\| \overrightarrow{J_{ij}^{V}} \right\|_2}{\left| \overrightarrow{V_V} \right|} \tag{8}$$

$$TS_i = t_i^P + t_i^C + t_i^T \tag{9}$$

$$t_i^T = \frac{R_i}{(\beta - L)} \tag{10}$$

$$L = \lambda \times \left(\frac{\beta - \beta_0}{d} \right) \times \left\| \overline{UMES} \right\|_2 \tag{11}$$

$$UT = \sum_{i,j \in N} TF_{ij} \times X_{ij} + \sum_{i \in N} TS_i \times \xi_i, \quad \forall i,j \in \{S,T,E\} \tag{12}$$

In Eq. (7), $\overline{V_U}$ is the speed vector of the UAV, where $\overline{V_H}$ and $\overline{V_V}$ are its components in the horizontal and vertical directions, respectively. In Eq. (8), TF_{ij} is the flight time of the UAV for track point $i \to j$, where $\left| \overline{V_H} \right|$ and $\left| \overline{V_V} \right|$ respectively indicate the magnitude of the speed component in the horizontal and vertical directions. In Eq. (9), TS_i is the inspection task execution time of the UAV at device i, where t_i^P is the attitude adjustment time of the UAV, t_i^C is the working time of the image sensor, and t_i^T is the information transmission time of the UAV. Equation (10) is used to obtain t_i^T, where R_i is the amount of task data to be transmitted at device i, β is the transmission speed without interference, and L is the interference loss. In Eq. (11), λ is the environmental interference coefficient, which is determined by the electromagnetic environment and equipment distribution of the substation. β_0 is the interference loss at reference distance d, $\left\| \overline{UMES} \right\|_2$ is the distance of the UAV from the receiver of the mobile edge server. ξ_i is a 0–1 variable, where $\xi_i = 1$ means that the UAV detects equipment point i and $\xi_i = 0$ means that the UAV does not detect equipment point i.

3.2.3 Inspection of energy consumption indicators

The energy consumption differs with the flight state of the UAV, and here, we only analyze the energy consumption in the hovering and general flight states. Since we mainly study the UAV inspection path, the complex dynamics analysis of the induced drag and wing drag of the UAV is ignored, and an energy consumption index of the substation UAV inspection is established from the relationship between the lift and power of the UAV established by Fan *et al.*[23] as follows.

In the hovering state,

$$Fl_H - G_U = 0. \tag{13}$$

In the general flight state,

$$Fl_N \times \sin \alpha - G_U = 0. \tag{14}$$

Here, Fl_H is the lift of the UAV in the hovering state and Fl_N is the lift of the UAV in the general flight state. G_U is the gravitational force acting on the UAV; $G_U = m_U \times g$, where m_U is the mass of the UAV and g is gravitational acceleration. α is the pitch angle of the UAV in flight.

On the basis of the study of Fan *et al.*,[23] the following approximate relationship is obtained between the lift and power of the UAV:

$$Fl = K \times \sqrt{P_{UF}} - C, \tag{15}$$

where K is the power conversion factor and C is a constant.

Combining Eqs. (13)–(15), the flight powers of the UAV in the hovering and general flight states are respectively given by

$$P_{UF}^H = \frac{1}{K^2}(Fl_H + C)^2 = \frac{1}{K^2}(G_U + C)^2, \tag{16}$$

$$P_{UF}^N = \frac{1}{K^2}(Fl_N + C)^2 = \frac{1}{K^2}\left(\frac{G_U}{\cos\alpha} + C\right)^2. \tag{17}$$

Combining Eqs. (8), (9), (16), and (17) yields the energy consumption index UE, which is the energy consumed by the UAV in completing all equipment inspections:

$$UE = (\sum P_{UF}^N \times TF_{ij} \times X_{ij}) + (\sum (P_{UF}^H + P_E) \times TS_i \times \xi_i), \quad \forall i, j \in \{S, 1, 2, \cdots, n\}, \tag{18}$$

where P_E is the total power of the sensors carried by the UAV.

3.2.4 Optimization objective

The aim of our research is to inspect substation equipment and collect and upload inspection data via UAVs, and the energy consumption or time of the operation should be minimized while guaranteeing the reliability of the inspection. Therefore, an objective function based on the established UAV inspection distance index, time index, and energy consumption index is established, as shown in Eq. (19), with the optimization objective of minimizing the total index. Figure 2 shows the schematic diagram of the UAV states.

$$F = \min(UD \times UT \times UE) \tag{19}$$
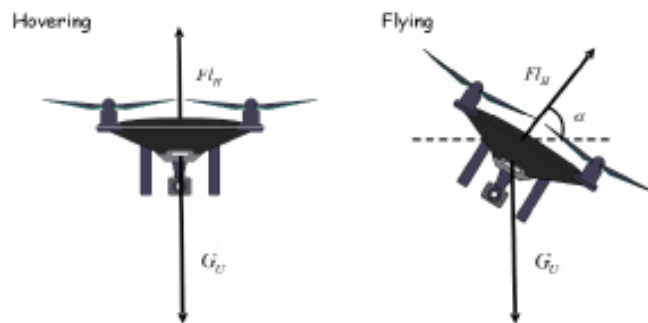
Fig. 2.   Schematic diagram of the UAV states.

3.2.5 Constraints

The sensor operation constraints, UAV physical performance constraints, and trajectory planning constraints for the entire inspection are as follows.

$$\sum_{i=1}^{n} X_{Si} = 1 \tag{20}$$

$$\sum_{i=1}^{n} X_{iE} = 1 \tag{21}$$

$$\sum_{i=1} X_{ij} = 1, \forall j \in \{1, 2, \cdots, n\} \tag{22}$$

$$\sum_{j=1} X_{ij} = 1, \forall i \in \{1, 2, \cdots, n\} \tag{23}$$

$$-5° \leq \alpha \leq 5° \tag{24}$$

$$\left\| \overrightarrow{UI_i^{max}} \right\|_2 \times \theta_U + \left\| \overrightarrow{UI_i^{min}} \right\|_2 \times \theta_D \geq h_i^{max} - h_i^{min}, \quad 0 \leq \theta_U \leq \theta_U^{max}, \quad -\theta_D^{min} \leq \theta_D \leq 0 \tag{25}$$

$$AV \leq \left\| \overrightarrow{UI_i^{max}} \right\|_2 \times \arccos(\overrightarrow{UI_i^{max}}, \overrightarrow{UI_i^u}) \leq AT, \quad I_i^u = (x_i, y_i, z_U) \tag{26}$$

$$UE_{max} - UE \geq P_{UF}^{N} \times TF_{GE} \tag{27}$$

$$\sum \xi_i = n, \quad \forall i \in \{1, 2, \cdots, n\} \tag{28}$$

Equations (20) and (21) ensure that the UAV departs from and returns to the inspection center. Equations (22) and (23) ensure that each point to be inspected is assigned a UAV for inspection. Equation (24) defines the pitch angle range of the UAV in the flight process that gives the UAV as high stability as possible during the inspection flight. According to the study of Xiang *et al.*,[24] the stability of the UAV increases when the pitch angle increases from 0 to 5° and decreases when the pitch angle increases from 5 to 10° . Furthermore, from Eq. (17), it can be seen that in the general flight state, the smaller the pitch angle of the UAV, the smaller the flight power. To increase the flight time, the pitch angle range of the UAV is specified as –5 to 5°. Equation (25) indicates that the UAV image sensor at device i can be acquired to cover the device, where θ_U and θ_D are the elevation angle and pitch angle of the UAV gimbal and θ_U^{max} and θ_D^{min} are the maximum elevation angle and maximum pitch angle of the UAV gimbal,

respectively. Equation (26) is the workable constraint of the image sensor of the UAV at device i, where AV is the minimum focusable distance of the visible sensor and AT is the maximum collectable distance of the IR sensor while guaranteeing the acquisition accuracy. Equation (27) is the UAV return constraint, where UE_{max} is the total energy, UE is the energy consumed to complete the inspection of all devices determined by Eq. (18), G is the last inspection point of the UAV, TF_{GE} is the return time of the UAV, and P_{UF}^N is the flight power. Equation (28) ensures that all devices are inspected.

4. Improved Trajectory Planning Algorithm

Because of its small size and robust mobility, a rotary-wing UAV can be used for effective targeting in substation inspection without major spatial constraints, making it easy to generate many feasible paths. In the path planning problem with multiple decision indicators and complex constraints, traditional path planning algorithms such as the artificial potential field method and GA have high computational complexity and poor solutions; thus, a more generalized path planning algorithm with a high-dimensional solution space is required. MA combines the major advantages of PSO, GA, and the firefly algorithm (FA). It has a high convergence speed while maintaining the accuracy of the solution; however, MA easily falls into a local optimal solution, which reduces the solution accuracy. Thus, we design a hybrid MA based on the improved RRT algorithm for UAV substation inspection path planning.

4.1 Improved RRT path planning algorithm

The traditional RRT algorithm plans paths mainly by randomly generating extended trees. Although the optimal path can be found if the number of searches is sufficient, the random strategy makes the algorithm search space large, the search efficiency is low, and the results of path planning obtained using RRT are highly random and the process is computationally complex. Therefore, to address the problem of the randomness of the traditional RRT algorithm, we improve the RRT algorithm by using an adaptive dynamic step size and the Gibbs sampling strategy, starting from the parent node selection and randomness.

4.1.1 Gibbs sampling strategy

Gibbs sampling is one of the random simulation sampling algorithms. If the specific density function of the probability distribution cannot be determined, an approximate solution can be obtained using Gibbs sampling, thus simplifying the problem and improving the computational efficiency. When Gibbs sampling is used, it is necessary to know the conditional probability of an attribute in the sample under all other attributes and then use this conditional probability to generate sample values of each attribute in the distribution. The Gibbs pseudocode is shown in Algorithm 1.

Algorithm 1
Gibbs pseudocode.

Algorithm 1 *Gibbs*
Input : *nSamples · mu · rho , propSigma,Ub,Lb*
Output : *x*
1 : *x ← zeros(nSamples,2)*
2 : *x(1,1) ← unifrnd(Lb(1),Ub(1))*
3 : *x(1,2) ← unifrnd(Lb(2),Ub(2))*
4 : *t ← 1*
5 : **while** *t < nSamples* **do**
6 : *t ← t+1*
7 : *T ← [t - 1,t]*
8 : **for** *each iD* $\in \left[1, dim \right]$ **do**
9 : *nIx = dims ~= iD*
10 : *muCond ← mu(iD) + rho(iD) * (x(T(iD),nIx) - mu(nIx))*
11 : *varCond ← sqrt(1 - rho(iD)²)*
12 : *x(t,iD) = normrnd(muCond,varCond)*
13 : **end**
14 : **end**

4.1.2 Adaptive dynamic step strategy

The application of the Gibbs sampling strategy reduces the randomness of the traditional RRT algorithm and effectively improves its search efficiency. However, owing to the fixed expansion step, in a scenario with dense obstacles, the algorithm cannot quickly and smoothly pass through the obstacles. To avoid the extended tree wandering around the same point for a long time, a self-learning strategy is introduced into the traditional RRT algorithm, and Eq. (30) is used to make the algorithm realize dynamic step adjustment. K varies with the number of iterations as follows:

$$K = \left(\frac{N_{iter}}{Max_{iter}} \right)^2, \tag{29}$$

where K is the dynamic step adjustment coefficient, N_{iter} is the number of times of Gibbs sampling, and Max_{iter} is the maximum allowable number of times of Gibbs sampling. The formula used to dynamically adjust the step size is

$$step_{size} = step_{size} - K \times step_{size} \ , \quad \text{if } N_{iter} > \gamma, \tag{30}$$

where $step_{size}$ is the step length of the RRT algorithm and γ is the threshold number of consecutive invalid nodes. K is introduced to adjust the step size according to γ, so that the step size changes dynamically with the number of calculations. Since the extended tree wanders for a long time near the same point, the range of passable paths near the point is small and the step size is too large for obstacle avoidance. Figure 3 shows how K changes with N_{iter}.

4.2 Traditional MA

MA is a metaheuristic algorithm based on the dynamic interaction of mayflies. Its main idea is to imitate the flight behavior and mating behavior of mayflies for related optimization work, and the intelligent behavior of mayflies mainly comprises the movement of female mayflies, the movement of male mayflies, and the mating process.

4.2.1 Movement of male mayflies

Adult male mayflies rise to the surface of the water to find a location to attract females. Their search for this location is modeled as

$$x_i^{t+1} = x_i^t + v_i^{t+1}, \tag{31}$$

$$v_{ij}^{t+1} = v_{ij}^t + a_1 e^{-\beta r_p^2}(pbest_j - x_{ij}^t) + a_2 e^{-\beta r_g^2}(gbest_j - x_{ij}^t), \tag{32}$$

where $x_i^0 \in U(x_{min}, x_{max})$, v_{ij}^t is the velocity of mayfly i in dimension $j = 1, ..., n$ at time t, x_{ij}^t is the position of mayfly i in dimension j at time t, and a_1 and a_2 are positive attraction constants for scaling the contributions of the cognitive and social components, respectively. $pbest_i$ is the global optimal solution, $gbest_i$ is the local optimal solution, β is the fixed visibility, and r_p and r_g are the Cartesian distances between x_i and $pbest_i$ and between x_i and $gbest_i$, respectively.

At the same time, the mayfly updates its velocity through the courtship dance, which is modeled by
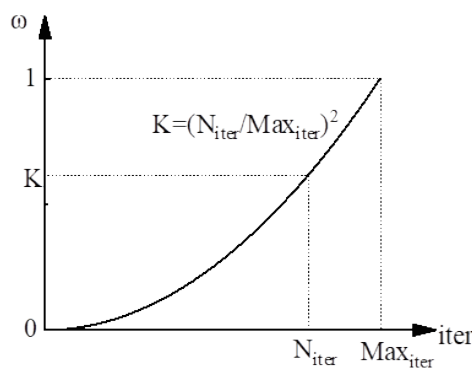
Fig. 3.   Graph showing change in K.

$$v_{ij}^{t+1} = v_{ij}^{t} + d * r, \tag{33}$$

where d is the distance coefficient and r is a random number in the range $[-1, 1]$.

4.2.2 Movement of female mayflies

Upon the arrival of the male mayfly, the female mayfly moves towards the male mayfly, which is modeled as

$$y_i^{t+1} = y_i^{t} + v_i^{t+1}, \tag{34}$$

$$v_{ij}^{t+1} = \begin{cases} v_{ij}^{t} + a_2 e^{-\beta r_{mf}^{2}} (x_{ij}^{t} - y_{ij}^{t}), & f(y_i) > f(x_i), \\ v_{ij}^{t} + fl * r, & f(y_i) \le f(x_i). \end{cases} \tag{35}$$

Here, y_{ij}^{t} is the position of female mayfly i in dimension j at time t, r_{mf} is the Cartesian distance between the female and male mayflies, and fl is the wandering coefficient.

4.2.3 Mating

One individual each from the male and female populations is selected as a parent to produce more adaptive offspring according to Eqs. (36) and (37).

$$offspring_1 = L * male + (1-L) * female \tag{36}$$

$$offspring_2 = L * female + (1-L) * male \tag{37}$$

Here, *male* denotes the male sire, *female* denotes the female sire, and L denotes a random value within a certain range.

4.3 Improved MA

The advantage of MA is that it combines the major advantages of PSO, GA, and FA, and there are various ways to update the positions of the population. However, it is still possible to fall into a local optimum. Therefore, the Cauchy mutation strategy and Lèvy flight strategy are introduced to extend the search space of the algorithm to improve its ability to find the global optimum.

4.3.1 Cauchy mutation strategy

In the mating behavior of the traditional MA, the search direction and weight coefficients of each dimensional variable change randomly and irregularly with the number of updates, which affects the stability of the algorithm in solving optimization problems. The Cauchy distribution has a stronger disturbance ability than the Gaussian distribution. For this reason, the Cauchy mutation strategy is introduced to update the positions of species offspring by using its perturbation ability to increase the biodiversity of the population while improving the stability of the algorithm to further improve its ability to find the global optimum.

The Cauchy mutation originates from the Cauchy distribution. The probability density of the 1D Cauchy distribution is

$$f(x) = \frac{1}{\pi} \cdot \frac{a}{a + x^2}. \tag{38}$$

When $a = 1$, the distribution is called the standard Cauchy distribution. Therefore, the formula for updating progeny in MA is

$$\begin{cases} offspring_1 = cauchy(0,1) \times |X_{male} + (1 - cauchy(0,1)) \times |X_{female}, \\ offspring_2 = cauchy(0,1) \times |X_{female} + (1 - cauchy(0,1)) \times |X_{male}. \end{cases} \tag{39}$$

4.3.2 Lèvy flight strategy

The Lèvy flight strategy was introduced to update the moving positions of female and male mayflies during the computation to enhance the ability of MA to calculate the global optimal solution. The formulas for the positions of mobile male and female mayflies after the introduction of the Lèvy flight strategy are respectively as follows:

$$\begin{cases} x_i^{t+1} = x_i^t + v_i^{t+1}, & 0.5 > rand \\ x_i^{t+1} = x_i^t + Levy(\beta)x_i^t, & 0.5 \leq rand \end{cases} \tag{40}$$

$$\begin{cases} y_i^{t+1} = y_i^t + v_i^{t+1}, & 0.5 > rand \\ x_i^{t+1} = x_i^t + Levy(\beta)x_i^t, & 0.5 \leq rand \end{cases} \tag{41}$$

where *Levy* is the optimized step size coefficient, which obeys the Lèvy flight distribution

$$Levy(\beta) \sim \frac{\beta \Gamma(\beta) \sin(\pi\beta/2)}{\pi} \frac{1}{s^{1+\beta}}, \tag{42}$$

where β is a constant taking values in the range of [0, 2]. In this paper, β is taken as 1.5. $\Gamma(\beta)$ is the gamma function and s is expressed as

$$s = \frac{\mu}{|\upsilon|^{\frac{1}{\beta}}}; \mu \sim N(0,\sigma^2), \upsilon \sim N(0,1), \tag{43}$$

where

$$\sigma = \left\{ \frac{\Gamma(1+\beta)}{\beta \cdot \Gamma\left((1+\beta)/2\right)} \cdot \frac{\sin(\beta\pi/2)}{2^{(\beta+1)/2}} \right\}^{\frac{1}{\beta}}. \tag{44}$$

4.3.3 Algorithm flow of ICLMA

The specific steps of the hybrid mayfly algorithm (ICLMA) based on the Cauchy mutation strategy and Lèvy flight strategy are as follows.

Step 1 Initialize mayfly populations $Mayfly_{i,iter}$ and $Mayflyf_{i,iter}$, set initial parameters, and define decision variables.

Step 2: Randomly generate female and male mayfly populations according to solution space and calculate initial fitness function value.

Step 3: Using random values, update moving positions of female and male mayflies by Eqs. (40) and (41), respectively.

Step 4: Calculate fitness function value of new position, as well as global variable position and target function value.

Step 5: Update female and male mayfly mating offspring positions according to Eq. (39) and calculate fitness function values.

Step 6: Check if updated global variable position has changed according to fitness function value, and update corresponding parameters.

Step 7: Check if number of iterations has reached the maximum. If not, return to Step 3.

As a summary, the flow chart of the improved RRT algorithm and ICLMA is shown in Fig. 4.

5. Simulation Experiments

We establish a 3D simulation environment model based on a substation in Yunnan, China, as shown in Fig. 5. The DJI Royal 2 rotary-wing UAV is selected to perform the substation inspection simulation. The rotary-wing UAV is equipped with a visible camera, IR sensor, RTK positioning module, and map transmission module to perform the inspection. Based on the established 3D environment model and the UAV inspection model, the designed ICLMA is used for path planning to verify the effectiveness of the proposed model and algorithm, and the relevant parameters of the simulation inspection task are shown in Table 1. MATLAB R2020a is used as the algorithm programming tool, the operating system is Windows 10, the computer memory is 32 GB, and the CPU is Intel i7-10870H.
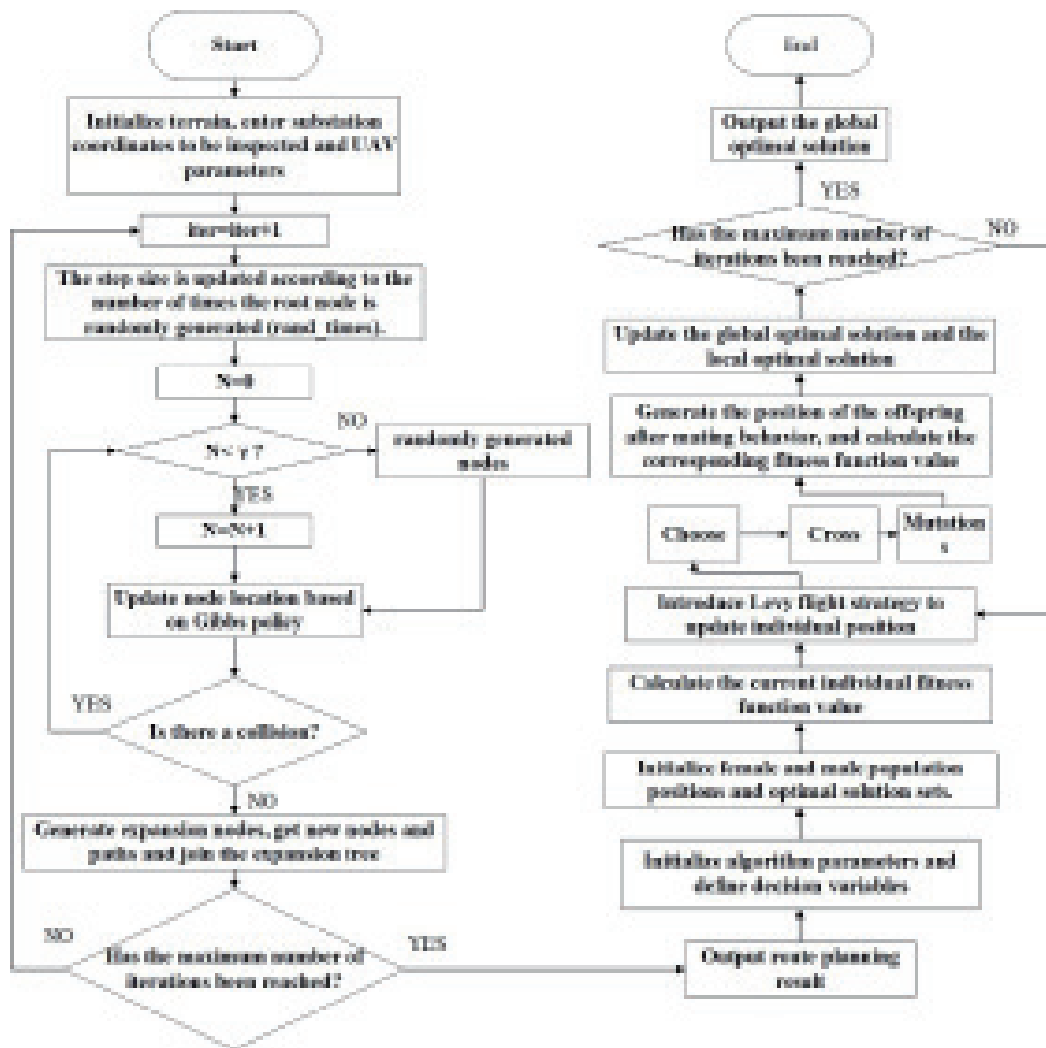
Fig. 4.   Flow chart of ICLMA.
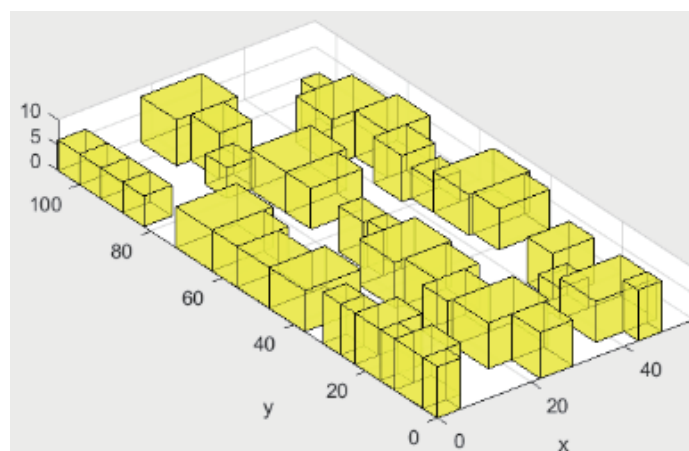
Fig. 5.   (Color online) Three-dimensional simulation environment model.

Table 1
Parameters related to simulation inspection.

Name	Value
Drone mass, m_{ij}	1100 g
Maximum ascent speed	4 m/s
Maximum descent speed	4 m/s
Maximum horizontal flight speed	14 m/s
Maximum flight altitude	6000 m
Maximum tiltable angle	25°
Maximum rotational angular speed	100°/s
UAV real-time image transmission speed, β	40 Mbps
Quality	720p, 30 Hz
Battery capacity	3850 mAh
Total energy	59.29 Wh
Rotatable range of head	Pitch −90–+30°
Angle jitter amount	±0.005°
Temperature measurement range	−40 to 550 ℃
Temperature measurement method	Spot temperature measurement Area temperature measurement
Visible camera focus	1 m to infinity
ISO range	Video: 100–12800 (auto) Photo: 100–1600 (auto)
Task volume per detection point, R_i	50 M
Gravitational acceleration, g	9.8
Power conversion factor, K	2.061
Constant, C	8.532

In addition, to compare the performance and robustness of the proposed algorithm, ICLMA, GA, PSO, and MA are run 100 times as experimental algorithms, and the results are compared and analyzed.

5.1　Results of substation inspection simulation

The simulation results after 100 runs are shown below, where Fig. 6 shows the optimal iteration profiles of GA, PSO, MA, and ICLMA over 100 runs; Fig. 7 shows the worst iteration profiles of GA, PSO, MA, and ICLMA over 100 runs; and Fig. 8 shows the average iteration profiles of GA, PSO, MA and ICLMA over 100 runs. Table 2 shows some of the parameters of the designed algorithm. Table 3 shows the average, optimal, and worst objective function values and the average running time of the four algorithms of GA, PSO, MA, and ICLMA for 100 runs.

The results are presented for a run randomly selected from the 100 runs. Figure 9 shows the iteration profiles of GA, PSO, MA, and ICLMA for the randomly selected run. Table 4 shows the path length, inspection time, and inspection energy consumption values for the randomly selected run. Figure 10 shows related indexes of each algorithm, and Fig. 11 shows the substation inspection paths generated by GA, PSO, MA, and ICLMA.
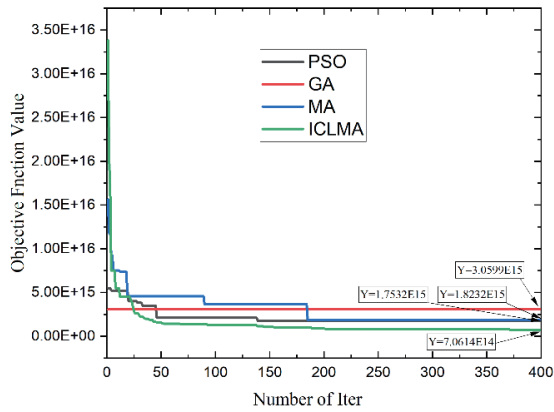
Fig. 6.   (Color online) Optimal iteration profiles of GA, PSO, MA, and ICLMA over 100 runs.
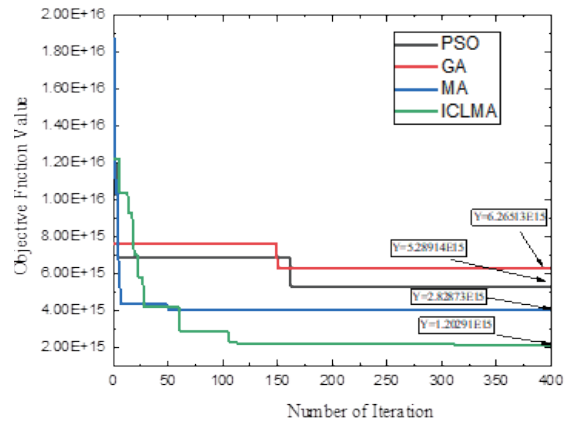
Fig. 7.   (Color online) Worst iteration profiles of GA, PSO, MA, and ICLMA over 100 runs.
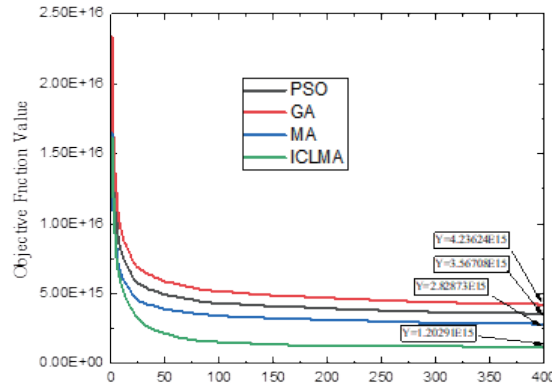
Fig. 8.   (Color online) Average iteration profiles of GA, PSO, MA and ICLMA over 100 runs.

Table 2
Simulation parameters.

Name	Value
Maximum number of iterations, Max_{iter}	400
Inertia weight, g	0.8
Inertia weight damping ratio $gdmap$	1
Global learning coefficient1, $a2$	1.5
Global learning coefficient1, $a3$	1.5
Global learning coefficient1, $a2$	1

Table 3
Results of GA, PSO, MA, and ICLMA runs.

Algorithm	Optimal	Worst	Average
GA	3.060×10^{15}	6.2651×10^{15}	4.2360×10^{15}
PSO	1.7532×10^{15}	5.2891×10^{15}	3.5670×10^{15}
MA	1.8232×10^{15}	3.9117×10^{15}	2.8287×10^{15}
ICLMA	7.0613×10^{14}	2.1198×10^{15}	1.2029×10^{15}
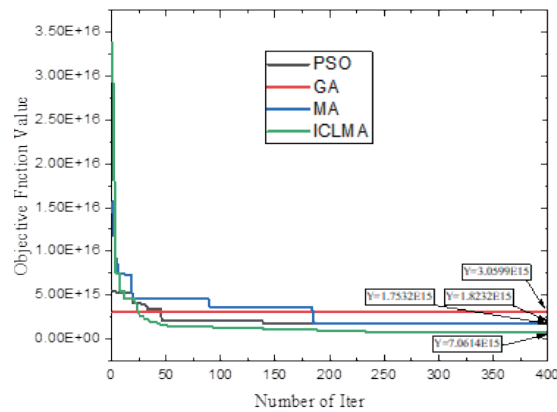
Fig. 9.   (Color online) Iteration profiles of GA, PSO, MA and ICLMA runs randomly chosen from 100 iterations.

Table 4
Specific simulation results.

Algorithm	Distance (m)	Time (s)	Energy consumption (W)
GA	4665.51	832.11	7.70×10^{11}
PSO	1861.89	637.17	2.53×10^{11}
MA	2420.95	683.76	1.73×10^{9}
ICLMA	1711.97	623.44	9.55×10^{8}
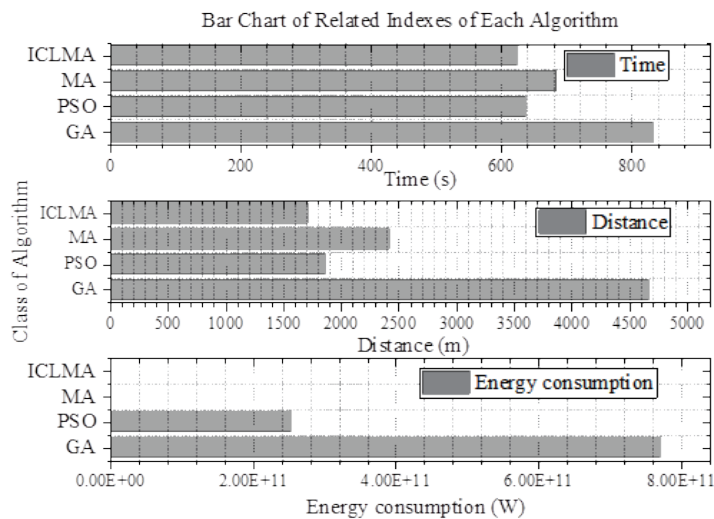
Fig. 10.   Bar chart of indexes of each algorithm.

5.2   Analysis of results

From Figs. 6–8, the designed ICLMA has a stronger search capability than GA, MA, and PSO, both in the early stage of the search and in the global search, and its convergence speed and accuracy are superior to those of the other algorithms. Moreover, from the comparison of the
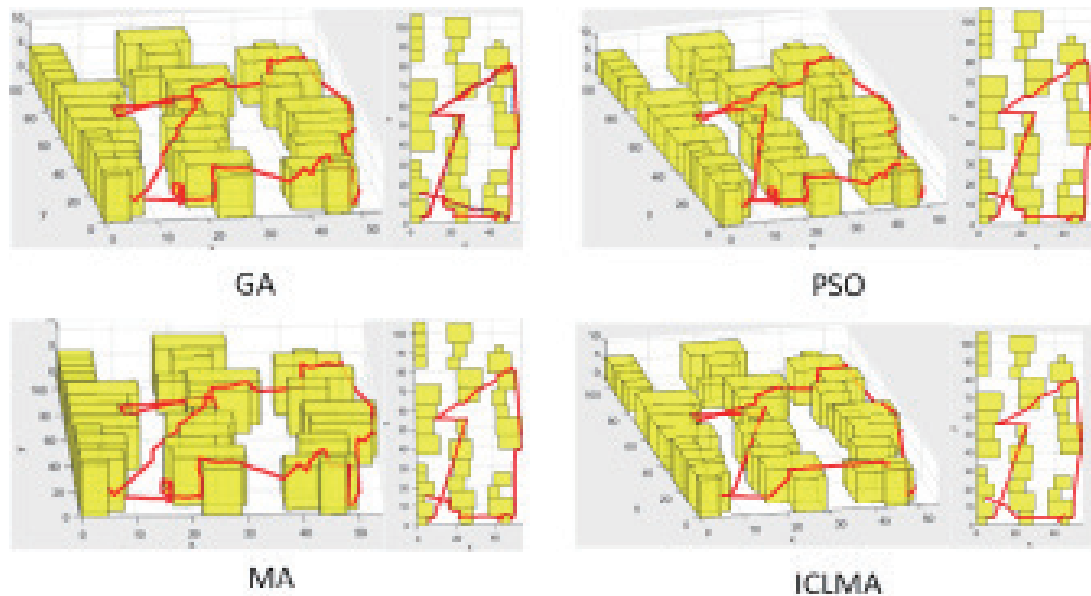
Fig. 11.   (Color online) Substation inspection paths generated by GA, PSO, MA, and ICLMA.

average, optimal, and worst objective function values of 100 runs in Table 3, the designed ICLMA algorithm reduces the objective function values by 57.48–71.60, 45.81–66.16, and 59.72–76.92% compared with those of GA, MA, and PSO, respectively. Furthermore, it can be seen from Fig. 9 that ICLMA still has a significant advantage over the other algorithms in the randomly selected run. From Fig. 10, the distance, time, and energy consumption of ICLMA are clearly superior to those of the other algorithms, and the energy consumption of ICLMA is so much smaller than those of GA and PSO that it does not appear in the figure. In addition, from the specific run results in Table 4, the total length of the inspection path of ICLMA is 1711.97 m, which are 63.31, 29.29, and 8.05% less than those of GA, MA, and PSO, respectively. The total time of inspection of ICLMA is 623.44 s, which is 25.08, 8.82, and 2.15% less than those of GA, MA, and PSO, respectively. In addition, the total energy consumption of inspection of ICLMA is 9.55×10^8 W, which is 99.8, 44.79, and 99.62% less than those of GA, MA, and PSO, respectively. In summary, the designed ICLMA has a strong global and local search capability and high robustness.

From the above results, the proposed inspection model comprehensively involves inspection length, time, and energy consumption and can effectively generate inspection paths. ICLMA also benefits from the introduction of improved strategies such as the Cauchy mutation strategy and Lèvy flight strategy, which can reduce the length, time, and energy consumption of inspection compared with those of the general trajectory planning algorithms, thus helping promote intelligent and efficient substation inspection.

6.   Conclusions

We investigated the substation inspection problem based on a rotary-wing UAV with fused heterogeneous sensors. A UAV inspection model with the minimum total index as the

optimization target was constructed under the premise of integrating the constraints at all physical levels and taking the inspection distance, time, and energy consumption as the optimization indexes. In addition, an RRT algorithm that introduces the Gibbs sampling strategy and adaptive dynamic step strategy was designed, a floating algorithm that introduces the Cauchy mutation strategy and Lèvy flight strategy was combined, and finally, the improved ICLMA for planning the inspection path was designed. Experiments based on a substation 3D simulation environment model were carried out, and PSO, GA, and MA were selected for cross-sectional comparison to verify the feasibility of the proposed model and algorithm. The experimental results show that the proposed model and algorithm can reduce the inspection distance, time, and energy consumption and help promote automated and intelligent substation inspection. In future research, we will further study UAV autonomous inspection based on communication networks such as 5G to further reduce the workload of personnel, and we will also focus on the inspection of substations in complex environments such as plateaus to extend the generalizability of the research.

Acknowledgments

References

1   M. A. Judge, A. Khan, A. Manzoor, and H. A. Khattak: J. Energy Storage **49** (2022) 104056. http://doi.org/10.1016/j.est.2022.104056

2   H. Liu, Y. Sun, J. Cao, S. Chen, N. Pan, Y. Dai, and D. Pan: IEEE Trans. Ind. Inf. **18** (2022) 5537. https://doi.org/10.1109/TII.2022.3142723

3   Y. Li, W. Long, and S. Wei: J. Xiangtan University (Natural Science Edition) **42** (2020) 118. https://doi.org/ https://doi.org/10.13715/j.cnki.nsjxu.2020.05.012

4   S. B. Slama: Ain Shams Eng. J. **13** (2022) 101504. https://doi.org/10.1016/j.asej.2021.05.018

5   J. Hu, Z. Zhu, X. Lin, Y. Li, J. Liu, and R. Shen: High Voltage Eng. **2** (2021) 230. https://doi.org/10.13336/j.1003-6520.hve.20200584

6   Z. Qadir, F. Ullah, H. S. Munawar, and F. Al-Turjman: Comput. Commun. **168** (2021) 114. https://doi.org/10.1016/j.comcom.2021.01.003

7   C. Yu, G. Wu, J. Zhang, X. Ji, and D. Qi: Autom. Instrum. **6** (2020). https://doi.org/10.19557/j.cnki.1001-9944.2020.06.008

8   D. Tran, T. X. Vu, S. Chatzinotas, S. ShahbazPanahi, and B. Ottersten: IEEE Trans. Veh. Technol. **69** (2020) 9483. https://doi.org/10.1109/TVT.2020.3001403

9   Y. Wang, W. Wang, F. Xu, J. Wang, and H. Chen: Trans. Chin. Soc. Agric. Mach. **51** (2020) 103. https://doi.org/10.6041/j.issn.1000-1298.2020.11.011

10   H. Liu, Q. Chen, N. Pan, Y. Sun, Y. An, and D. Pan: IEEE Trans. Ind. Inf. **18** (2022) 582. https://doi.org/10.1109/TII.2021.3054172

11   M. Tang, Y. Gu, S. Wang, and Q. Liang: Rob. Auton. Syst. **119** (2019) 247. https://doi.org/10.1016/j.robot.2019.07.008

12   S. Lu, Y. Zhang, and J. Su: IEEE/CAA J. Autom. Sinica **4** (2017) 830. https://doi.org/10.1109/JAS.2017.7510364

13   X. Dong, S. Ji, J. Zhu, and B. Yang: Power System Protect. Control **18** (2021). https://doi.org/10.19783/j.cnki.pspc.201581

14   Y. Wang, H. Cengm, R. Zhao, Y. Xv, and Y. Zhang: Electr. Eng. **16** (2021). https://doi.org/10.19768/j.cnki.dgjs.2021.16.036

15 P. Kumar, S. Garg, A. Singh, S. Batra, N. Kumar, and I. You: IEEE Internet Things J. **5** (2018) 1698. https://doi.org/10.1109/JIOT.2018.2796243

16 N. Wen, L. Zhao, X. Su, and P. Ma: IEEE/CAA J. Autom. Sinica. **2** (2015) 173. https://doi.org/10.1109/JAS.2015.7081657

17 J. Pan, J. Lv, L. Yan, S. Weng, S. Chu, and J. Xue: Math. Comput. Simul. **193** (2022) 509. https://doi.org/10.1016/j.matcom.2021.10.032

18 X. Chai, Z. Zheng, J. Xiao, L. Yan, B. Qu, P. Wen, H. Wang, Y. Zhou, and H. Sun: Aerosp. Sci. Technol. **121** (2022) 107287. https://doi.org/10.1016/j.ast.2021.107287

19 Y. Wang, P. Bai, X. Liang, W. Wang, J. Zhang, and Q. Fu: IEEE Access **7** (2019) 105086. https://doi.org/10.1109/ACCESS.2019.2932008

20 K. Zervoudakis and S. Tsafarakis: Comput. Ind. Eng. **145** (2020). https://doi.org/10.1016/j.cie.2020.106559

21 Z. Liu, P. Jiang, J. Wang, and L. Zhang: Expert Syst. Appl. **177** (2021). https://doi.org/10.1016/j.eswa.2021.114974

22 Z. Zhou, C. Zhang, C. Xu, F. Xiong, Y. Zhang, and T. Umer: IEEE Trans. Ind. Inf. **14** (2018) 2705. https://doi.org/10.1109/TII.2018.2794320

23 Y. Fan, K. Shen, D. Wang, C. Zhai, and H. Zhang: Trans. Chin. Soc. Agric. Mach. **10** (2020). https://doi.org/10.6041/j.issn.1000-1298.2020.10.005

24 C. Xiang and J. Mao: Comput. Simul. **10** (2021). https://doi.org/10.3969/j.issn.1006-9348.2021.10.010